Yb3+- and CaF2 nanocrystallites-containing oxyfluorogermanotellurite glass-ceramics

Hayat Zanane, Matias Velázquez, Dominique Denux, Philippe Goldner, Alban Ferrier, Aïcha Kermaoui, Hamid Kellou, Michel Lahaye, Sonia Buffiere, François Weill

Yb^{3+}- and CaF_2 nanocrystallites-containing oxyfluorogermanotellurite glass-ceramics

Hayat Zanane[a,d,*], Matias Velázquez[a], Dominique Denux[a], Philippe Goldner[b], Alban Ferrier[b,c], Aïcha Kermaoui[d], Hamid Kellou[d], Michel Lahaye[e], Sonia Buffière[a], François Weill[a]

[a] CNRS, Université de Bordeaux, ICMCB, UPR 9048, 87 avenue du Dr. A. Schweitzer, 33608, Pessac cedex, France
[b] PSL Research University, Chimie ParisTech - CNRS, Institut de Recherche de Chimie Paris, 75005, Paris, France
[c] Sorbonne Universités, Facultés des sciences et ingéniérie, UFR 933, 75005, Paris, France
[d] Faculté de Physique, Laboratoire d'Électronique Quantique, USTHB, BP 32 El alia, 16111, Bab Ezzouar, Alger, Algeria
[e] PLACAMAT, UMS 3626, CNRS-Université Bordeaux, 87 avenue du Dr. A. Schweitzer, 33600, Pessac, France

Keywords:
Glass materials
Yb^{3+} ion spectroscopy
Rare-earth materials
Optical glass ceramics

A B S T R A C T

A new 30 GeO_2-30 TeO_2-15 ZnO-10 Na_2CO_3-10 CaF_2-3 La_2O_3-2 YbF_3 glass composition was synthesized and submitted to several heat treatments to provoke nanocrystallization in its bulk. The formation of nanocrystallites was evidenced by high resolution transmission electron microscopy and X-ray diffraction, and their nature and size was characterized. The spectroscopic and magnetic properties of the Yb^{3+} ions dissolved in the glass and, presumably, in the nanocrystallites, were investigated by absorption and emission spectroscopies (including anti-Stokes emissions from Tm^{3+} and Er^{3+} impurities), fluorescence transients and magnetic susceptibility measurements. It was found that the Yb^{3+} ions experimental lifetime and average effective magnetic moment, as well as Tm^{3+} and Er^{3+} ions anti-Stokes emission intensities, increase with increasing crystallization state of the initial glass.

1. Introduction

The glass-ceramics containing nanocrystals doped with rare-earth ions are more and more investigated in several domains. In this type of materials, the combination of the best optical properties of single crystals, and of the low fabrication cost (easiness of synthesis and glass formation), broadened their field of potential applications, for example in medical technologies, photovoltaics, optical telecommunications and lasers [1–4]. During the last decade, an increasing interest in TeO_2-based matrices has risen, because of their remarkable properties. As compared with phosphate and silicate glasses, tellurite glasses have lower phonon energies [5,6], lower melting point temperature, larger infrared transparency, good thermal and mechanical stabilities, high chemical durability and larger refractive index [5,7–14]. The addition of fluorine into the glass composition further decreases the matrix phonon energies (to typically $\sim 500\,cm^{-1}$) and favors the formation of fluorinated nanocrystals in an oxide matrix. It is expected that the resulting optical properties will be improved by the incorporation of rare-earth ions in the nanocrystalline domains of the glass-ceramics. In this work, we address the case of GeO_2-strengthened TeO_2-based glass matrices. The addition of GeO_2 gives rise to interesting structural units and consequently, it affects the physical, thermal and optical properties of the tellurite glass network. For instance, an increase of the chemical durability, the UV–visible transmission and the thermal stability [15] can be foreseen. Calcium oxide and/or fluoride (CaO/CaF_2) were used as glass modifiers because of their adequate contributions to the glass formation. Besides, in several well-known luminescent host matrices, it was reported that a rare-earth ions can be substituted for Ca^{2+} cations [16–19], on the other hand the addition of fluorine compounds, such as BaF_2 or CaF_2, to RE^{3+}-doped tellurite glasses helped removing OH^--groups and increased the RE^{3+} ions fluorescence lifetime [20-23]. Among the rare-earth ions, Yb^{3+} ones are known to display a very simple energy level diagram, constituted of only two spin-orbit multiplets, the degeneracy of which are split by the surrounding crystal field. This eventually leads to simple absorption and emission spectra in the near infrared spectral range due to magnetic dipole and forced electric dipole transitions [24].

In this study, we present the visible and near IR spectroscopic properties of Yb^{3+}-doped oxyfluorogermanotellurate glass ceramics, which have been heat treated in order to form nanocrystallites embedded into the glass matrix. The latters were characterized by X-ray diffraction (XRD), high-resolution transmission electron microscopy

* Corresponding author. CNRS, Université de Bordeaux, ICMCB, UPR 9048, 87 avenue du Dr. A. Schweitzer, 33608, Pessac cedex, France.
E-mail address: hzanane@usthb.dz (H. Zanane).

(HRTEM) and EDS chemical analysis, and attempts at measuring the change of crystal field exerted by the Yb^{3+} ions nearest and next nearest neighbours when passing from the glass to the nanocrystallite domains were performed by optical spectroscopies and magnetic susceptibility measurements.

2. Experimental

The nominal molar composition of oxide and oxyfluoride glasses prepared in this work was: 30 GeO_2-30 TeO_2-15 ZnO-10 Na_2CO_3-10 $CaCO_3$-3 La_2O_3-2 Yb_2O_3 (G-GTO), and 30 GeO_2-30 TeO_2-15 ZnO-10 Na_2CO_3-10 CaF_2-3 La_2O_3-2 YbF_3 (G-GTOF). The glasses were elaborated by conventional melting, the starting powders being weighed in the desired amounts according to the selected compositions with an accuracy of ± 1 mg. After grinding, the powders were placed in a covered platinum crucible and melted for 1 h at 1050 °C and 1100 °C for the oxyfluoride and oxide glass, respectively. The melts were then rapidly quenched into a preheated stainless steel thin plate at T_g-20 °C to avoid thermal shock. The glass was subsequently heat-treated at T_g-20 °C, in order to relax the mechanical stresses arising from the quenching. Finally, the glasses were polished for structural, optical and spectroscopic measurements. The as-prepared oxyfluoride glasses were heat treated at 713 K (30 min), 713 K (2 h) and 728 K (2 h) to synthesize transparent glass ceramics. The Yb^{3+} contents were determined by Electron Dispersive Spectroscopy (EDS) and Electron Probe MicroAnalysis/Wavelength Dispersion Spectroscopy (EPMA/WDS), over large distances in four different samples and found to be sufficiently uniform to be averaged in each sample: 5.67 ×, 5.80 ×, 5.84 × and 5.49 × 10^{20} $Yb^{3+}.cm^{-3}$ concentrations were found. In the remainder of this paper, we shall use an average concentration of 5.70 × 10^{20} $Yb^{3+}.cm^{-3}$. The composition of the glasses (Na, Ca, Zn, Ge, Te, La, O, F) was determined by EPMA/WDS, in order to allow for the energy resolution of the Ca-K_α (3.691 keV) and Te-L_α lines (3.769 keV), and of F-K_α (0.677 keV) and La-M lines (0.833 keV, even if for La we used the L line at 4.651 keV). Indeed, the EDS energy resolution is 137 eV, while that of EPMA/WDS is a few tens of eV. The main differences observed between the initial and the final compositions (see Table 1 of the supplementary information file, hereafter called SI) are likely to be due to losses by sublimation and volatilization of TeO_2 during the initial heating and melting stage of the precursor glass (the vapour pressure of TeO_2 is higher than 0.3 atm at temperatures higher than 905 K [25,26]). For the differences in F content, YbF_3 and CaF_2 are not volatile but they oxidize in air at high temperature.

The differential thermal analysis of the glasses were performed by means of a differential thermal analyzer DTA Model SDT Q600 TA instrument, with a heating rate of 10 K/min. The samples were heated in alumina crucibles from room temperature to 1300 K under N_2 atmosphere with a 100 ml/min flow. The X-ray diffraction was carried out in a powder diffractometer (PANalytical X'pert Pro) in the 2θ range 10–80° with Cu K_α radiation (λ = 1.54056 Å) operating at 40 kV and 30 mA. The scanning rate was 0.0028°/s. The transmission spectra were recorded by means of a UV–Vis–NIR VARIAN Cary 5000 spectrophotometer in the 400–2000 nm spectral range. The IR absorption spectra were measured with a BRUKER Equinox 55 spectrophotometer. Density measurements were performed by ultrapycnometry using a Helium QUANTACHROME Ultrapyc 1200e Pycnometer. We made three measurements for each sample. Each measurement took 1 h and gave us twenty values, so that we averaged sixty values to find the density of each sample. For the base glass and the three heat treated samples (30 min at 713 K, 2 h at 713 K and 2 h at 728 K), the following values were obtained: 4.68, 4.67, 4.68, 4.65 g/cm^3, respectively.

We used a high-resolution transmission electron microscope (HRTEM, JEM-2200FS) equipped with energy-dispersive spectrometer (EDS) system to analyze the microstructure and the elements' distribution of treated glasses. The EDS mappings and spectra were recorded in scanning TEM (S-TEM) mode with a focus spot of 1.5 nm.

The magnetic susceptibility was measured in field heated and cooled modes (10 K/mn) using an EZ-7 MICROSENSE Vibrating Sample Magnetometer operated in the 295–930 K temperature range under an applied magnetic field of 1–1.8 T. Several glass samples of mass typically between 25.7 and 105.2 mg were cemented on a quartz rod, the diamagnetic contribution of which was also measured and subtracted from our data. When arrived at the highest temperature selected for each sample, a 10 min stage was imposed to the sample and then, the measurement in cooling mode was started.

Room temperature Stokes and Anti Stokes fluorescence decay measurements were performed using an OPO laser (EKSPLA) tuned to the desired excitation wavelength (e.g. 980 nm). The photoluminescence (PL) signal was then collected from the perpendicular direction and sent to the spectrometer (Princeton Acton 2300) combined with a photomultiplier tube (Hamatsu R928) or an InGaAs photodiode. The infrared PL of Yb^{3+} ions have been recorded under 908 nm excitation provided by a Coherent 829 Ti:Sapphire laser. The PL signal was detected with an InGaAs photodiode using a lock-in amplifier.

3. Results and discussion

3.1. Thermal stability of G-GTO and G-GTOF glasses

The DSC curves of the two glasses are shown in Fig. 1. Table 1 summarizes the thermal properties of our germanotellurite glasses together with selected compositions published in the literature for the purpose of developing the crystallization of CaF_2 in tellurite glasses.

The change in thermal behavior was first noticed in the base glass melting temperature, 1323 K for G-GTOF and 1373 K for G-GTO, unlike tellurite glasses that can melt at temperatures as low as 1073 K. The oxide glass scanning calorimetric curve establishes the high thermal stability of this glass network, resulting in the high glass transition temperature T_g = 749 K, and we did not observe any crystallization peak up to 1023 K. The introduction of GeO_2 is known to modify the skeleton of the telluride glasses. These characteristic values show the interest of studying this composition as an amorphous glass, but not as a glass ceramics. So, for the purpose of investigating this system as a glass ceramics, we have substituted CaO and Yb_2O_3 by CaF_2 and YbF_3, respectively. The thermal analysis curve of the oxyfluoride composition clearly shows the appearance of an exothermic phenomenon starting at 741 K. This peak is due to the crystallization of the phase nucleated thanks to fluorine elements, which makes this composition a good precursor glass for the development of nano-structured glasses. As

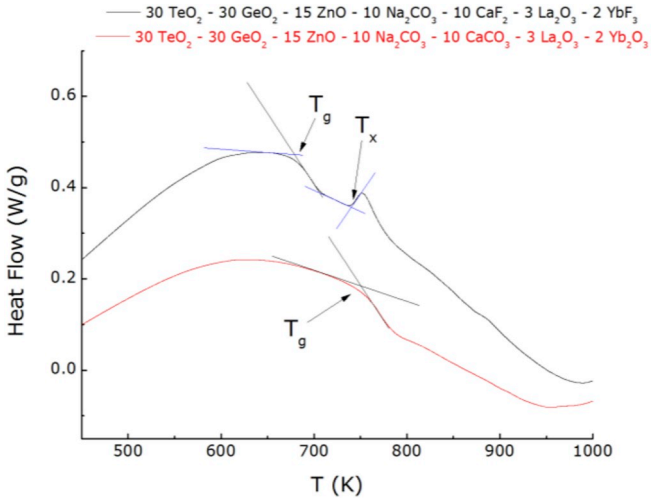

Fig. 1. DSC curves of the G-GTO and G-GTOF glass samples prepared in this study.

Table 1
Thermal properties of the oxide and oxyfluoride glass samples. T_g, T_x and T_c represent the glass transition temperature, the starting point of crystallization temperature, the crystallization temperature, respectively, and $\Delta T = T_x - T_g$.

Glass	T_g(K)	T_x(K)	T_c(K)	ΔT(K)
30 GeO_2-30 TeO_2-15 ZnO-10 Na_2CO_3-10 $CaCO_3$-3 La_2O_3-2 Yb_2O_3 (G-GTO)	749	/	/	≥597
30 GeO_2-30 TeO_2-15 ZnO-10 Na_2CO_3-10 CaF_2-3 La_2O_3-2 YbF_3 (G-GTOF)	679	741	753	335
Tellurite [27]	683	743	813	333
Telluro-silicate [28]	643	683	713	313

shown above in Table 1, the results obtained are similar to those published previously in oxy-fluorinated glasses based on tellurite [27,28], and also in aluminum silicate [16,17,29–34].

3.2. X-ray diffraction (XRD) on heat treated glasses

The crystallization of the nanocrystallites was favoured in the heat treated CaF_2-modified and YbF_3-doped glass. Using the Scherrer formula $L = \lambda/(\beta \times \cos(\theta))$ (with L the size of the crystallites in nm, $\lambda = 1.54056$ Å, β the integral width of the diffraction peak in radians and θ the Bragg angle (°)) [35], the average diameter of crystallites could be calculated, and found to measure between 3 and 10 nm in the three heat treated samples. In Fig. 2, we mention the (hkl) indices corresponding to the Fm-3m cubic phase of $Ca_{0.8}Yb_{0.2}F_{2.2}$ (ICSD 82712). The lattice spacings determined by XRD are averages over typically several tens of microns in the samples. It is obvious that other diffraction peaks appear on the diffractogram. This means that CaF_2 nanocrystallites could be of lower symmetry, or that there are different nanocrystallites phases. We did not manage to find a lattice unit cell which matches exactly these diffraction peaks alone.

The Williamson-Hall analysis carried out on the series of peaks assumed to be due to cubic CaF_2 (in Fig. 1 of the SI), in order to study the source of the broadening (sizes of crystallites and microconstraints) and the nature of this broadening (isotropic or function of Miller indices) [36], was too difficult to perform with our data. It might however be possible that in the glass ceramics heated at 728 K for 2 h the microstresses are isotropic ($\varepsilon = 10.9*10^{-3}$) with an average size of 12 nm of crystallites.

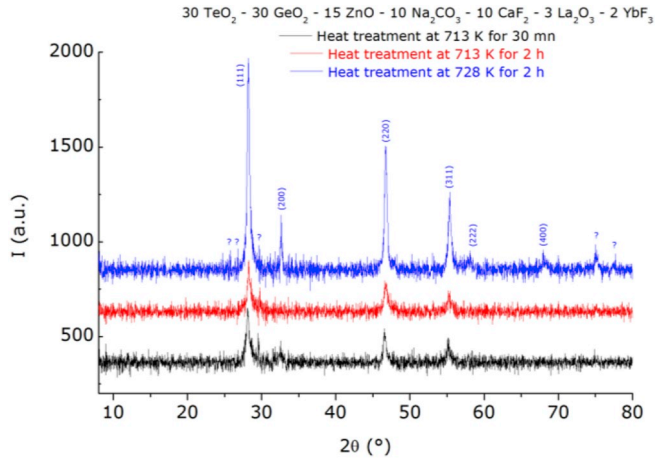

Fig. 2. X-ray diffraction patterns of three heat treated G-GTOF glasses. The indexation mentioned in the blue diffractogram corresponds to the Miller indices of the $Ca_{0.8}Yb_{0.2}F_{2.2}$ cubic phase Fm-3m. (For interpretation of the references to colour in this figure legend, the reader is referred to the Web version of this article.)

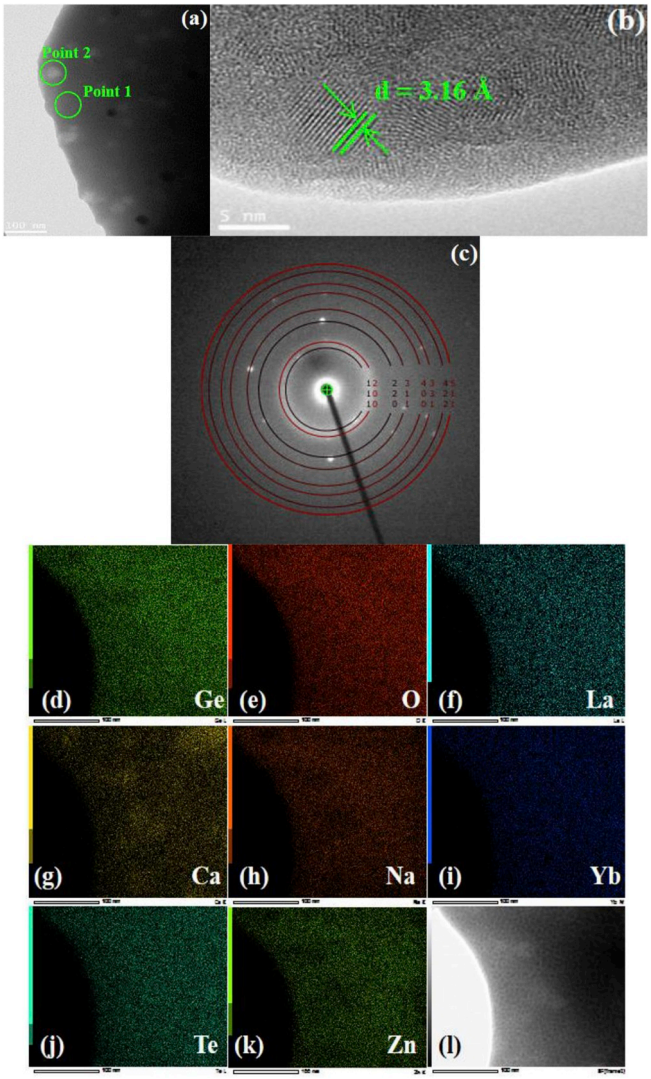

Fig. 3. (a) TEM, (b) HRTEM image. (c) SAED pattern of heat treated sample at 728 K for 2 h, (d-k) two-dimensional compositional elemental mappings of Ge, O, La, Ca, Na, Yb, Te, Zn and (l) the STEM image corresponding respectively.

3.3. High-resolution transmission electron microscopy (HRTEM), selected area electron diffraction (SAED) and EDS analysis of heat treated G-GTOF glasses

Fig. 3 (a) shows the TEM image of a G-GTOF glass sample treated at 728 K for 2 h, which unveils the formation of quasi-circular nanocrystals with an average size of 8 nm. This is consistent with the values calculated by means of Scherrer and of Williamson formulas applied to our XRD data (Fig. 2). Fig. 3 (b) shows the HRTEM image of single nanocrystals which exhibit atomic rows with calculated lattice spacings ranging from 3.16 to 3.23 Å, and from 2.74 to 2.80 Å. If we assume that these nanocrystals are made of cubic Fm-3m CaF_2, the latter spacings might be attributed to $d_{[111]} = 3.155$ Å and $d_{[200]} = 2.731$ Å, which turn out to be the two largest lattice spacings of diffracting planes in this crystal structure [37,38]. This could mean that the nanocrystallites observed already have a close-to-equilibrium habit, which would be rather surprising since 80 Å correspond to only ~15 unit cells of this crystal structure. Setting aside distance measurement error bars issues, the fact that some of the atomic interplane distances are slightly higher than those found in pure CaF_2 might be due to the partial substitution of Ca^{2+} cations for Yb^{3+} ones [39]. If we insert the Végard's law for the $Ca_{1-x}Yb_xF_{2+x}$ solid solution in the calculation of $d_{[111]}$ and $d_{[200]}$, we

deduce that the maximum amount of Yb^{3+} ions in these nanocrystallites is x ≈ 0.0375, or ≈8.61 × 10^{20} Yb^{3+}.cm^{-3}. Other lattice spacings between 3.5 and 3.8 Å were sometimes found in a few images, a little bit too short to be safely attributed to (110)-planes. The SAED pattern corresponding to the nanocrystals is shown in Fig. 3 (c). The theoretical ring pattern of CaF_2 has been superimposed to the experimental one. Clearly, the experimental reflections are consistent with the presence of CaF_2 nanocrystals. To investigate the distribution of Yb and of the other elements in the glass matrix, EDS spectra were recorded in different domains of the glass, excluding and including the nanocrystals (point 1 and point 2 shown in Fig. 3 (a)). The spectrum recorded at point 2 shows higher content of F and Ca than the one recorded in exactly the same conditions at point 1. On the other hand, the amounts of Ge, Te, Na, Zn, La and O are slightly lower, which suggests that the point 2 domain is composed of CaF_2. It was not possible to check if there is an Yb^{3+} concentration variation between points 1 and 2. The O, La, Ca, Na, Yb, Te, Zn and Ge two-dimensional compositional elemental mappings are shown in Fig. 3 (d) to 3 (k). The image for Ca element exhibits contrasts in the nanocrystallized domains which are complementary of the contrasts observed in the same places on the images for La, Na, Zn and Ge, which brings support to the contention that the nanocrystallites are Ca-based. The Ca atomic content increases by a factor ≈3.6 when the nanocrystallite is targeted by the electronic beam. Even if the surrounding amorphous matrix also contributes to the EDS signal, such an increase in Ca is larger than the sum of the uncertainties (see Table 2 of the SI file). The F element being lighter, it was not possible to check the same trend by this technique. Fig. 3 (d) to 3 (k) were also measured in another part of the sample and the same trend was observed (see in Fig. 2 of the SI). Comparative measurements between matrix and "nanocrystallite" zones were repeated and another example is given in Fig. 3 of the SI. Note that the HRTEM images in Fig. 3 (b) are local views at the nanometer scale, while the electronic "pear" that permits to quantify the elemental composition by EDS in scanning TEM mode in Fig. 3 of the SI file crosses the sample over all its thickness, ~100 nm.

3.4. Absorption and emission spectroscopies

Fig. 4 shows the transmission spectra and their calibration into absorption spectra, as well as the stimulated emission spectra obtained by reciprocity method (RM) [40–42], for the G-GTOF glass and glass ceramics (for the three heat-treatment). The germanotellurite glasses exhibit a large transmission window that extends from 320 nm to 6.2 µm. A slight red-shift of the bandgap could be observed in the glass ceramics with respect to the base glass, likely to be due to the light diffusion induced by the formation of the nanocrystallites. Broad absorption bands centered around 3300 nm (3600-2500 cm^{-1}) and 4300 nm (2260 cm^{-1}) might be assigned to vibrational modes of free hydroxyl groups OH^-, and of tellurium-bonded (Te—OH) groups [43–54]. These hydroxyl groups probably come from the residual water present in the starting products. No noticeable differences between the absorption spectra of the different samples can be observed in the 875–1100 nm domain. All samples exhibit the same absorption peak cross-section at λ_{ZP} = 976 nm, ≈1.5 × 10^{20} cm^2. Such a peak value is a clear indication that Yb^{3+} cations are located on noncentrosymmetric sites. Although the analysis of the baseline suggest that some light diffusion in the near UV and visible spectral ranges seems to be correlated to the heat treatment of the glasses, the absorption spectra do not stress any difference between the samples. All the glasses are doped with the same amount of Yb^{3+} and the local changes of the glass "structure" and elements around Yb^{3+} cations may not affect the crystal field parameters responsible for this intraconfigurational absorption transition, $^2F_{7/2} \rightarrow {}^2F_{5/2}$.

The $^2F_{5/2}$ multiplet radiative lifetime calculated with these absorption spectra, taking a degeneracy ratio of the $^2F_{5/2}$ and $^2F_{7/2}$ multiplets $g(^2F_{5/2})/g(^2F_{7/2})$ = 3/4 and an average wavelength 958.8 nm, is about 525.8 µs. This value is not correct because the 4th crystal field sublevel of the ground state is virtually unpopulated at room temperature. Such a small value must be corrected by means of Auzel's method [51]. Indeed, by calculating the oscillator strength and the spontaneous emission probability with, in his notations [55], α = 15.054 × 10^{-21} cm^2, β = 7.673 × 10^{-21} cm^2, γ = 1.695 × 10^{-21} cm^2, δ = 0 cm^2, and estimated $Z(^2F_{5/2})$ = 1.40263 and $Z(^2F_{7/2})$ = 1.37566 multiplet partition functions at room temperature,

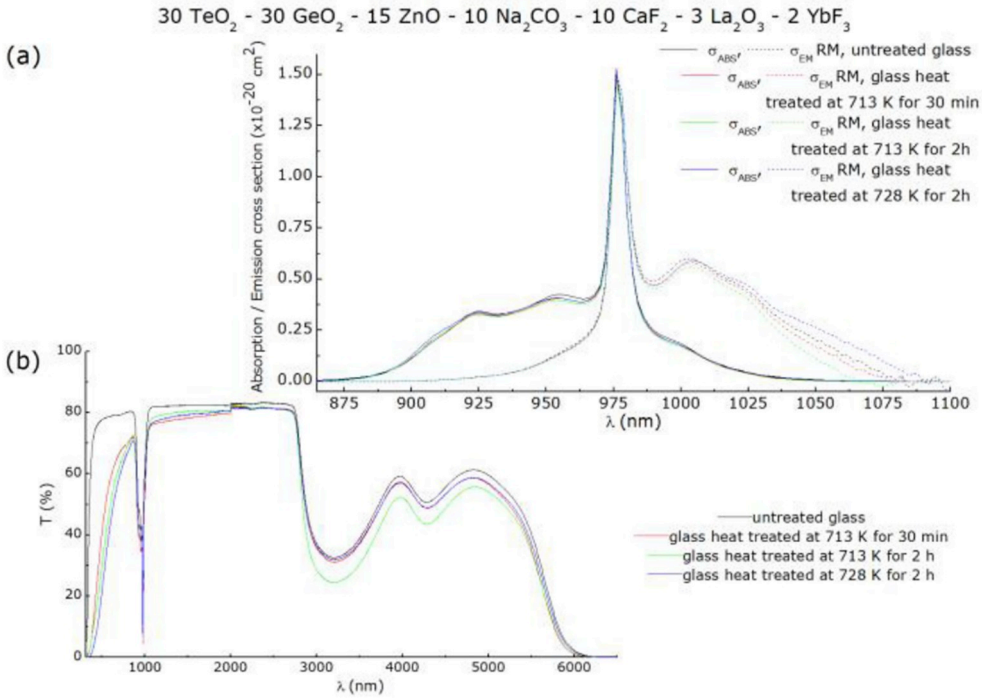

Fig. 4. (a) Absorption and emission cross-sections of G-GTOF glass and glass ceramics; (b) Transmission spectra of the same samples.

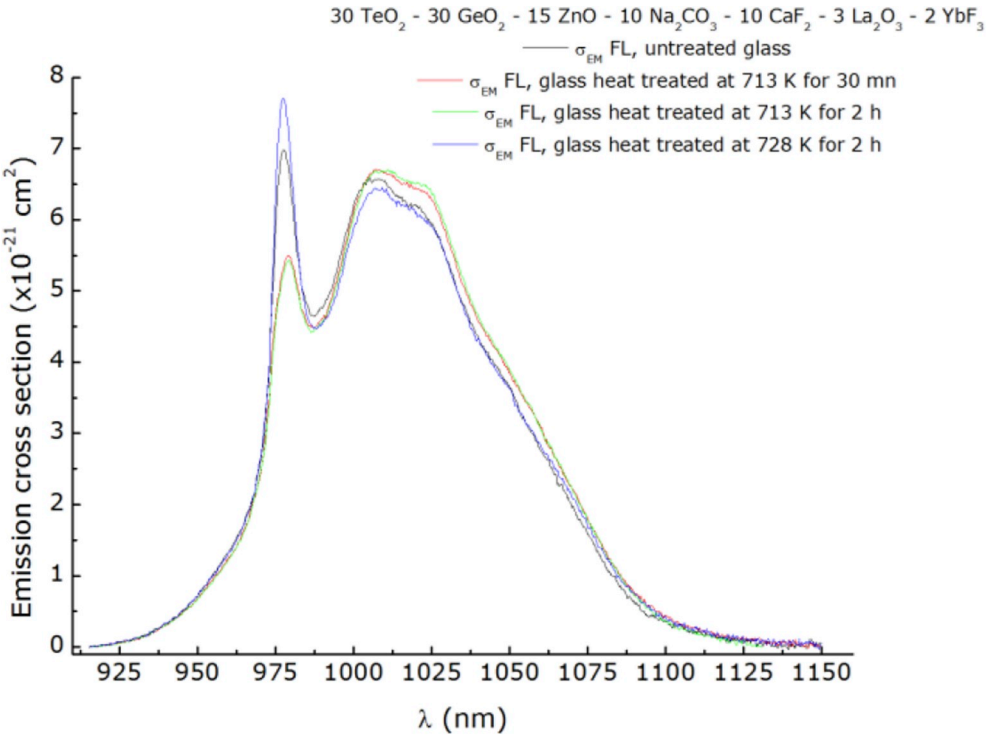

Fig. 5. Emission cross-sections of G-GTOF glass and glass ceramics, calibrated by the Fuchtbauer-Ladenburg method in the near infrared spectral range.

we find $g(^2F_{5/2})/g(^2F_{7/2}) = 0.9756$, hence a radiative lifetime of 683.6 µs. When we compare these numbers, as well as the shape of the spectra, with those of heavily Yb^{3+}-doped rare-earth sesquioxides crystals [24,56,57], and among them more particularly $(Gd,Yb)_2O_3$ crystals, we see that the Yb^{3+} $^2F_{5/2}$ radiative lifetime in the glass ceramics is much shorter than in the rare-earth sesquioxide single crystals. The main reason for this is that the $1 \rightarrow 6$ and $1 \rightarrow 7$ optical transitions (in the notations of [57]) have a peak cross-section much higher in the crystals than in the glasses. Needless to say, the broadness of the absorption bands is higher in the glass ceramics spectra than in the crystals' ones. However, the resulting integrated absorption cross-section is only a little bit higher in the glass ceramics than in the rare-earth sesquioxide single crystals. Note also that the forced electric dipole contribution to the $^2F_{7/2} \leftrightarrow {}^2F_{5/2}$ transition oscillator strength, $f^{ED}/f^{MD} \approx 9.4$, is intermediate between the one found in flux-grown $Gd_{1.72}Yb_{0.28}O_3$ (~11) and $Y_{1.87}Yb_{0.13}O_3$ (~8.8) crystals [24,56,57], which means the covalency of the bonds in the neighborhood of Yb^{3+} cations in the glass ceramics compares more favourably with that of the Y_2O_3 matrix than that of the Gd_2O_3 or Lu_2O_3 (~8.4) matrices.

Fig. 5 displays the Fuchtbauer-Ladenburg calibrated Yb^{3+} emission cross-section spectra derived experimentally, by exciting the crystal around 907 nm, with the radiative lifetime of 683.6 µs and an optical index of 1.91 (deduced from Fig. 4 (b)). The emission bands are so broad that they are not resolved. The emission cross-section of the zero-phonon line, at 977.5 nm, is the highest in the most crystallized sample, but the effect remains rather weak. The radiative lifetime refined in such a way that the emission spectra, calibrated in cross-section units by the Fuchtbauer–Ladenburg (FL) formula and by the reciprocity method, match approximately together at the zero-phonon wavelength, is ≈ 317 µs. This is only 46% of the correct radiative lifetime determined above and a clear indication of reabsorption in the sample. The modification of the spectra shown in Fig. 5 is also likely to be due to reabsorption and obviously, the reabsorption effect is the strongest at this wavelength. The Yb^{3+} cations absorption and emission spectra shown in Figs. 4 and 5 are dictated by the crystal field they undergo, and above all by the fact that it does not contain an inversion point symmetry operator. When the local site they lie at is noncentrosymmetric, the point group which leaves invariant the crystal field Hamiltonian is determined by the unit cell content in the crystallites, or by the nearest and next nearest neighbours of the Yb^{3+} ions in the glass. Indeed, the B_q^k crystal field parameters introduced in the parameterized Hamiltonian, scale as $< r^k > \times A_q^k$, where $A_q^k \propto \Sigma(Z_L e^2/R_L^{k+1})$, $< r^k >$ represents a distance typically of the unit cell dimension, k = 3, 5 and 7, and R_L is the Yb^{3+}-O^{2-}/F^- distance.

3.5. *Yb^{3+} ions fluorescence decays in the G-GTOF glass and glass ceramics*

Yb^{3+} ions fluorescence decays under resonant excitation shown in Fig. 6 can be fitted to an exponential law over time ranges which vary with the state of crystallization. In the untreated glass, the decay can be said to be simply exponential over ~3 times the radiative lifetime value, while in the heat treated glasses, the decay is exponential over ~4.5 times the radiative lifetime value. The resulting experimental lifetimes are longer in the heat treated glasses than in the untreated glass. Nevertheless, it should be mentioned that the heat treated samples data plotted in log-scale display a slightly concave curvature at very short times, followed by a linear decrease over ~3 ms in the three heat treated samples, which in the most heated glass sample forced us the start the fit at 1 ms. The increase in experimental lifetime might be explained by the progressive dissolution of the Yb^{3+} ions into the fluorine phase, which is characterized by low phonon energies (typically $\leq 500\ cm^{-1}$), and/or by a slight modification of the refractive index (because the CaF_2 optical index is lower than that of the glass). It turns out that the experimental lifetime exceeds by some 15 and 40% the radiative lifetime in the glass and the nanocrystallized samples, respectively, which, given the presence of OH^--groups and efficient energy transfer upconversion mechanisms towards Tm^{3+} and Er^{3+} impurities, is likely to be due to a strong reabsorption effect around 976 nm. The fluorescence transients displayed in Fig. 6 also depend on the local occurrence of an inversion symmetry (which would increase the experimental lifetime to tens of ms), on the strength of couplings likely to reduce the experimental lifetime and affect the shape of the decay (electron-phonon coupling, energy transfers, etc.), on reabsorption effects due to the absorption length at 976 nm (here ~1.17 mm), etc.

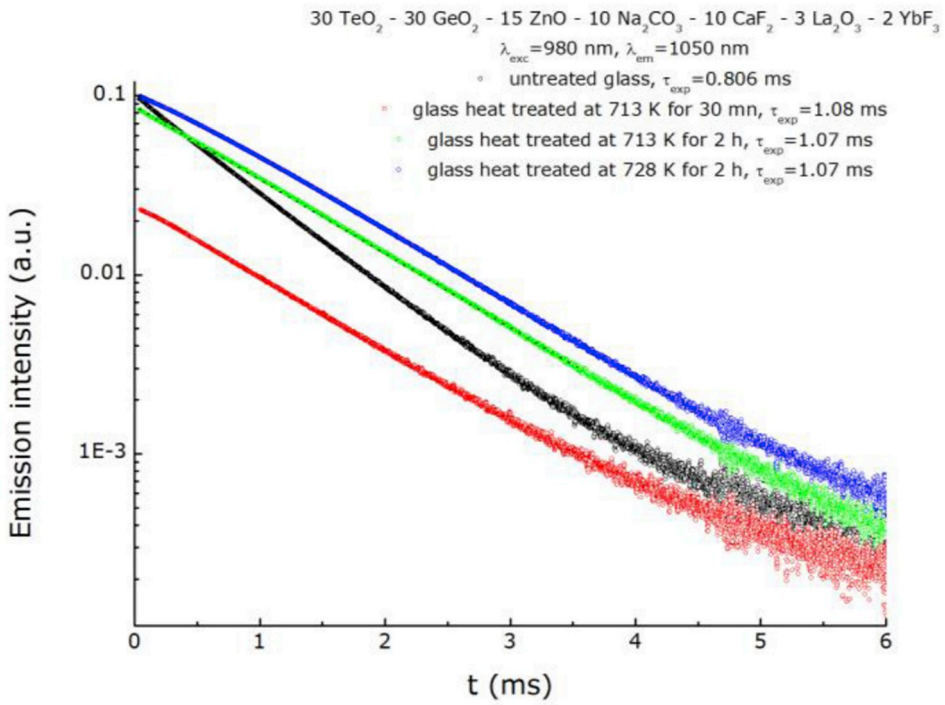

Fig. 6. Yb^{3+} ions fluorescence decays at λ_{em} = 1050 nm (under λ_{exc} = 980 nm) in G-GTOF glass and glass ceramics heat treated in different conditions.

3.6. Anti-Stokes emission spectra, Er^{3+} and Tm^{3+} impurity ions fluorescence transients in G-GTOF glass and glass ceramics

Anti-Stokes emission (AS) observed in the Yb^{3+}-doped materials may have different origins (cooperative emission from Yb^{3+}-ions pairs [58], upconversion by Yb-RE energy transfer mechanisms [59–61]). The anti-Stokes emission spectra and corresponding transients in Figs. 7 and 8 probe energy transfers which occur by dipole-dipole ($\propto 1/r^6$), dipole-quadrupole ($\propto 1/r^8$) and quadrupole-quadrupole ($\propto 1/r^{10}$) interactions, r being the distance between Yb^{3+} and other RE^{3+} impurity cations. Note that if we assume a perfectly isotropic Yb^{3+} concentration, the average distance between these cations is ≈ 7.5 Å, and if we assume the same kind of impurity RE^{3+} cations concentration, with a realistic one thousandfold amount less, the average distance between these RE^{3+} cations is ≈ 75 Å. So basically, energy transfer related characterizations are short to middle range probes. Fig. 7 shows the anti-Stokes (AS) emissions observed in the G-GTOF glass untreated, and glass ceramics heated at 728 K for 2 h. These emission spectra, which

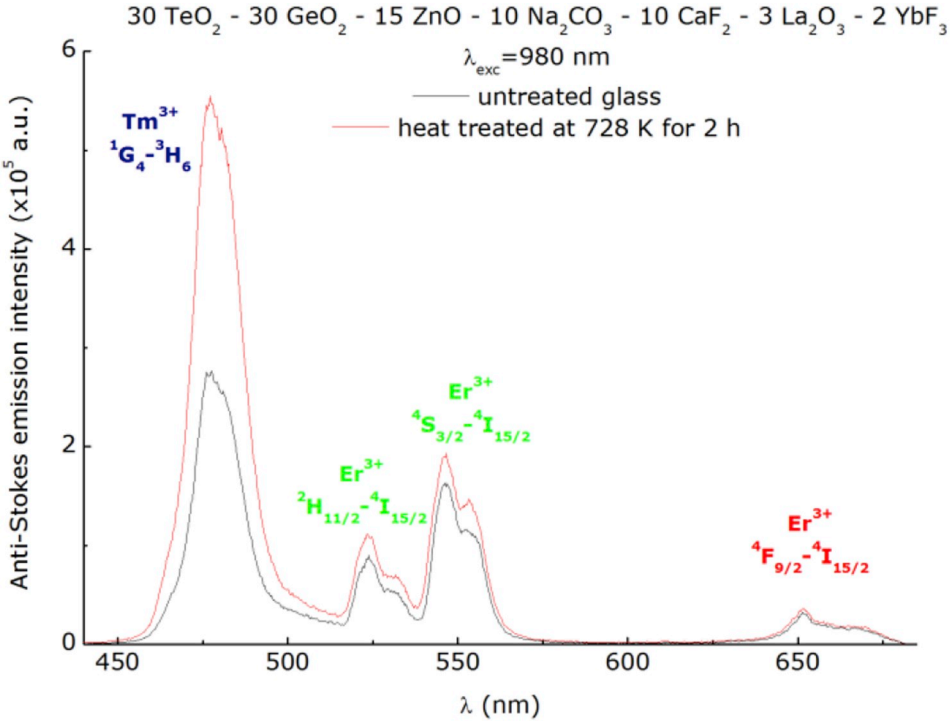

Fig. 7. Anti-Stokes emission spectra obtained under excitation at 980 nm, of Yb^{3+}-doped untreated G-GTOF glass, and glass ceramics treated at 728 K for 2 h.

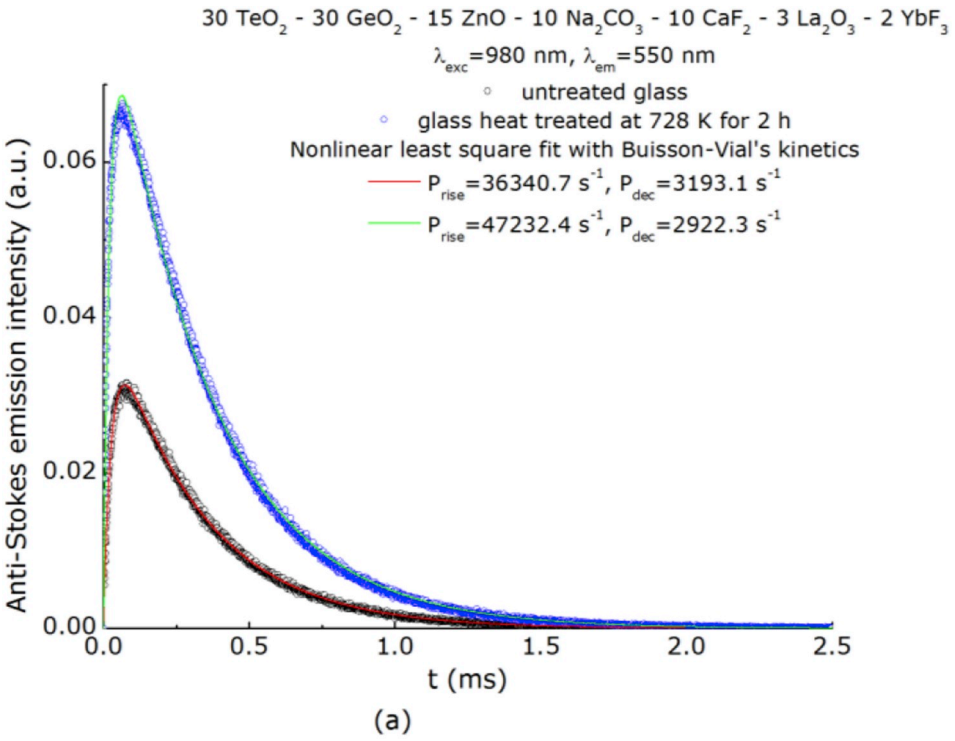

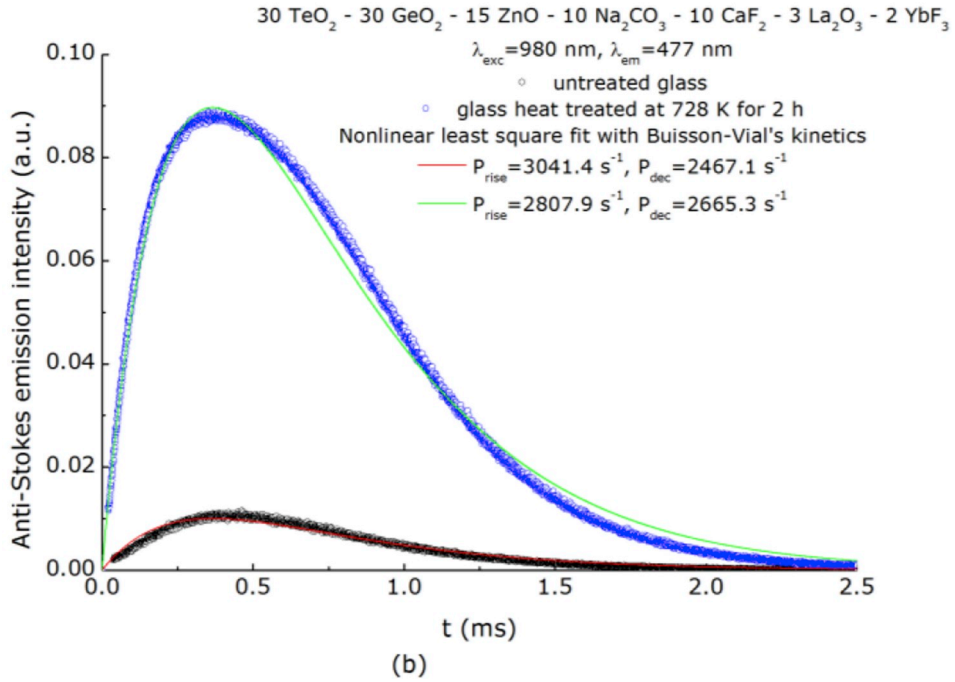

Fig. 8. Er^{3+} $^4S_{3/2}$ (a) and Tm^{3+} $^1G_4$ (b) room temperature anti-Stokes fluorescence transients in Yb^{3+}-codoped untreated glass and heat treated glass at 728 K for 2 h, obtained under excitation at 980 nm.

were obtained by exciting Yb^{3+} cations at λ = 980 nm, clearly show emission bands at 477 nm, 524 and 546 nm, and 652 nm. These AS emission bands are due to the $^1G_4 \rightarrow {}^3H_6$ transition of Tm^{3+} impurities, $^2H_{11/2} \rightarrow$ and $^4S_{3/2} \rightarrow {}^4I_{15/2}$ transitions of Er^{3+} impurities, and $^4F_{9/2} \rightarrow {}^4I_{15/2}$ transitions of Er^{3+} impurities. As compared with the same spectra in $(Gd,Yb)_2O_3$ crystals [57], in the glass ceramics, several features can be highlighted: (i) Tm^{3+} seems to be a prominent impurity; (ii) the emission bands are broader; (iii) the energy spacing between the Er^{3+} $^2H_{11/2}$ and $^4S_{3/2}$ multiplets is larger (the $^2H_{11/2}$ energy position is 12 nm below that in the flux-grown $(Gd,Yb)_2O_3$ crystals). In addition, we observe an increased intensity in AS emissions in the heat treated sample, especially for the Tm^{3+} impurities, perhaps due to selective dissolution of Yb^{3+} cations in the nanocrystallites (favouring energy transfer efficiency between these ions and other RE^{3+} cations). Rare-earth clustering is a well known phenomenon in CaF_2, which increases the rates of transfers.

Er^{3+} ($^4S_{3/2}$) and Tm^{3+} ($^1G_4$) fluorescence transients under non resonant excitation at 980 nm in the G-GTOF glass untreated, and in glass

Table 2
Energy transfers probabilities found by fitting the Tm^{3+}-$^1G_4$ and Er^{3+}-$^4S_{3/2}$ luminescence non resonant transients with Buisson-Vial's kinetics model.

Emitting level\sample	G-GTOF base glass (s^{-1})	G-GTOF heat treated glass (s^{-1})
Tm^{3+}-$^1G_4$	P_{rise} = 3041 P_{decay} = 2467	P_{rise} = 2808 P_{decay} = 2665
Er^{3+}-$^4S_{3/2}$	P_{rise} = 36341 P_{decay} = 3193	P_{rise} = 47232 P_{decay} = 2922

ceramics heated at 728 K for 2 h, are shown in Fig. 8(a) and (b). They exhibit two main features: (i) an intensity rise with a finite characteristic time due to the multiple photon absorptions, intermediate non radiative decays and Er^{3+} $^4S_{3/2}$ and Tm^{3+} $^1G_4$ multiplets experimental lifetimes; (ii) once the intensity maximum is reached, a non exponential decay with a decay time related to the Yb^{3+} $^2F_{5/2}$ multiplet lifetime (typically $\tau_{exp}/2$). Since the rise time and the average decay times for both ions are on the order of a few hundreds of μs, it is clear that under high excitation powers, or at high Er^{3+} and Tm^{3+} concentrations, such mechanisms are likely to deplete the Yb^{3+} $^2F_{5/2}$ multiplet and to increase the heat load released in the materials. As a first approach, we could approximately fit these transients with Buisson–Vial's kinetic model [62] and find the transfers probabilities gathered in Table 2.

3.7. Magnetic susceptibility of Yb^{3+}-doped glass and glass ceramics

Another way to investigate the potential impact of structural changes near the Yb^{3+} cations is to measure the magnetic susceptibility of the glass and the glass ceramics as a function of temperature, and cycling around the crystallization temperature. Fig. 9 shows the magnetic susceptibility measurements (in the MKSA units system) of YbF_3-doped untreated glass and of glass ceramics. We can deduce from our optical spectroscopy data that the crystal field energy splitting is at least 480.3 cm^{-1} (≈691 K) for the ground state $^2F_{7/2}$ (the 4th doublet energy position of which may tentatively be placed at 706.4 cm^{-1}), and 564.9 cm^{-1} (≈812.8 K) for the excited state $^2F_{5/2}$. These energy splitting ranges compare to the thermal activation energy scanned in our measurements (300–950 K), and are much higher than the magnetic characteristic energy due to the applied magnetic field, typically $Jg_J\mu_B\mu_0H/k_B \sim 9.7$ K.

These energy considerations explain why none of the magnetic susceptibility curves shown in Fig. 9 could be fitted to a Curie-Weiss law from room temperature to 800 K. The decrease of the magnetic susceptibility with increase of temperature is not simply hyperbolic, not even by successive segments. We could obtain a nice fit of the first heating curve, from RT to 800 K, with Van Vleck's expression for the paramagnetic susceptibility, simplified in such a way that the α_J constants, which contain temperature-independent high-frequency paramagnetic and diamagnetic contributions, are nil (expression 16 of chapter IX of reference [63], with the Yb^{3+} ions concentration given in the experimental section and the following crystal field energy level positions for the $^2F_{7/2}$ multiplet: 0, 265.9 and 480.3 cm^{-1}, the fourth level not being included in the refinement procedure). Note that 800 K is 50° above the crystallization temperature. The resulting average "L + 2S" effective magnetic moment from this fit is 3.4 μ_B/Yb^{3+}. This value corresponds to 75% of the theoretical free ion value. Above 800 K, the magnetic susceptibility behavior becomes of Curie–Weiss type, as suggested by the inverse of magnetic susceptibility, and the approximate magnetic moment increases to 3.9 μ_B/Yb^{3+}. The change in behavior is correlated with both crystallization and progressive thermal population of the four crystal field energy levels, which are Kramers doublets, of the ground state. After a 10 min period at 923 K, the cooling magnetic susceptibility curve turns out to be very close to that of the first heating, suggesting that the local structural changes of the Yb^{3+} cations are minor, or that there are not enough Yb^{3+} cations in the nanocrystallites to be detected, or that the sample was not enough crystallized. Consequently, we performed the same experiment with an YbF_3-doped glass already treated for 2 h at 753 K. The magnetic susceptibility curve, corrected for density variation with crystallization, exhibits a similar simplified Van Vleck behavior (α_J's = 0) from 300 to 829 K, with an increase of the average effective magnetic moment, 4.1 μ_B/Yb^{3+}. This value corresponds to 90% of the theoretical free ion value. Above 830 K, the behavior becomes of Curie–Weiss type but the range of temperature investigated is not large enough to ascertain the approximate magnetic moment tentatively obtained, ~5.7 μ_B/Yb^{3+}. Interestingly, while in the first derivative of the magnetic susceptibility curve for the untreated base glass, it was not possible to observe any

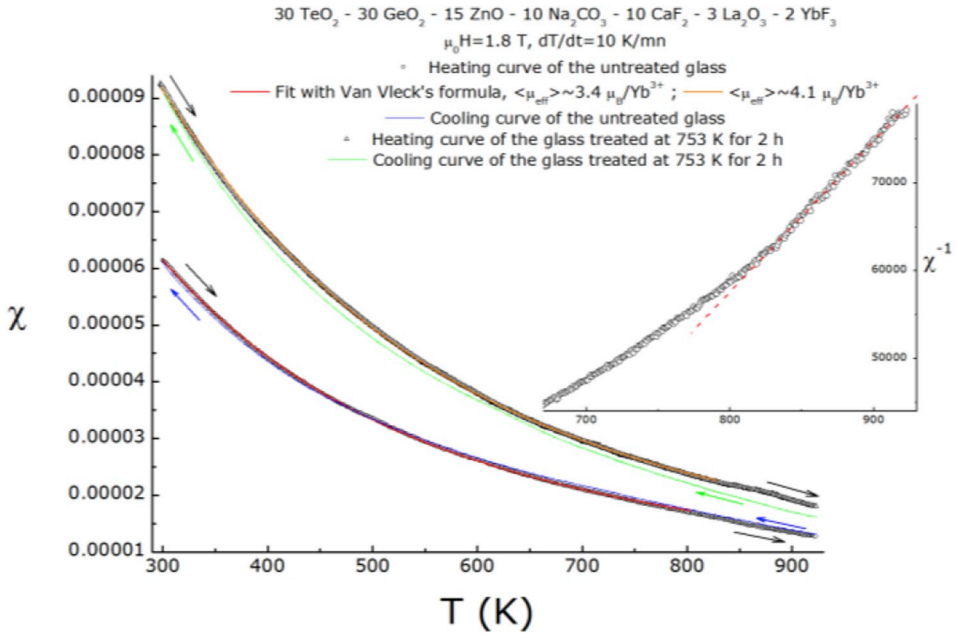

Fig. 9. MKSA magnetic susceptibility of an YbF_3-doped base glass and a heat treated at 753 K (2 h) glass, and zoom of the high temperature inverse magnetic susceptibility of the glass.

peak, in the first derivative of the magnetic susceptibility curve for the heat treated samples, we did observe several peaks at ~765 K and ~881 K upon heating, ~770 K and ~848 K upon cooling. The same kind of "crossover" from Van Vleck to Curie-Weiss behaviors, when the highest Kramers doublet becomes thermally populated, was observed in samples that were initially doubly doped in Yb^{3+} (by introduction of 2 Yb_2O_3 or of 4 YbF_3), with average effective magnetic moments close to 4.7 μ_B/Yb^{3+} up to 800 K, and Curie-Weiss behaviors above 800 K with slightly higher magnetic moments and an Yb^{3+} concentration extracted from the fit of about 1.3×10^{21} $Yb^{3+}.cm^{-3}$. It is well known that the crystal field Hamiltonian does not act on the spin, which is why such an optical transition as the one shown in Fig. 4 (a) is expected to occur at constant S ($\Delta S = 0$). On the spectra shown in Figs. 4 (a) and 5, the odd components of the crystal field dictate the cross-section values, especially the peak cross-section values and the transition strength, while the even B_q^k crystal field parameters (k = 2,4,6) determine the energy position of the peaks. Odd components are nonzero because the point group symmetry of the Yb^{3+} cations does not contain any inversion point symmetry operator. On the other hand, the inhomogeneous broadening of the peaks is mainly due to the local disorder in the glass network, averaged over a distance $\alpha_{ABS}{}^{-1} \sim 1.17$ mm at 976 nm in our samples. By acting on the Yb^{3+} $4f^{13}$ electrons energy levels diagram, the crystal field also modifies the effective magnetic moment of Yb^{3+} ions, and so their paramagnetic susceptibility behavior. Strictly speaking, the spin, orbital momentum and total angular momentum quantum numbers, are no longer the correct quantum numbers. It is the crystallographic quantum number which labels correctly the Kramers doublet levels arising from the splitting of the spin-orbit multiplets by the crystal field. Hence, the magnetic susceptibility measurements presented in Fig. 9 perform an average over all the Yb^{3+} cations distributed in the whole volume of the sample, which is completely crossed by the magnetic field. Even if T_g and T_c could not be directly detected on the magnetic χ versus temperature curve, a consistent increase in average effective magnetic moment with the crystallization state was evidenced.

So far, we can classify the techniques employed in sections 3.2 to 3.7 as follows: long range probe -XRD, VSM-, middle range probe −S-TEM mode EDS, energy transfer and transient spectroscopies-, local probe -absorption and emission spectroscopy, HRTEM-. XRD and HRTEM evidenced the formation of nanocrystallites in our samples and determined their characteristic dimensions, ≈80–100 Å. A tentative interpretation of some of the lattice spacings, together with EDS compositional elemental mapping, led us to have strong presumptions for Yb^{3+}-doped CaF_2 nanocrystallites formation. The dissolution of some of the Yb^{3+} cations in the nanocrystallites was suggested by the increase of their average effective magnetic moment and of their experimental emission lifetime with increasing degree of glass crystallization. Anti-Stokes emission intensity, especially of the $^1G_4$ Tm^{3+} ions, also increases with increasing degree of glass crystallization but this fact, given the dimensions of the nanocrystallites, is not easy to correlate to the potential dissolution of RE^{3+} impurity ions in the nanocrystallites. Absorption spectroscopy data did not help identifying the presence of Yb^{3+} cations in the nanocrystallites. In order to have chances to distinguish Yb^{3+} ions in the glass from Yb^{3+} ions in the nanocrystallites, it would have been necessary to perform site selective spectroscopy by pump-probe techniques that is, techniques which are both spectrally and time resolved. As a matter of fact, Yb^{3+} cations dissolved in CaF_2 crystals also give rise to broad absorption and emission spectra, due to the diversity of point defects that are likely to form.

4. Conclusions

A new Yb^{3+}-doped oxyfluorogermanotellurate glass has been synthesized and submitted to varied heat treatments to provoke crystallization in its matrix. The nanocrystallites formed have been found to measure typically 80–100 Å and, presumably, be of ~1.2 mol. % Yb^{3+}-doped CaF_2, by XRD, HRTEM, EDS, emission spectroscopy, emission lifetime and magnetic susceptibility measurements techniques. In particular, it was established that the experimental emission cross-section at 977.5 nm increases up to 7.7×10^{-21} cm^2, that the experimental lifetime reaches 1.07 ms and that the average effective Yb^{3+} cations magnetic moments are the highest in the most crystallized samples. Absorption spectra in cross-section units were also obtained and preliminary energy levels positioning was performed. The glass and glass ceramics contain significant amounts of Tm^{3+} and Er^{3+} impurities, as demonstrated by anti-Stokes emissions and their non resonant transients.

5. Declaration of interests

☒ The authors declare that they have no known competing financial interests or personal relationships that could have appeared to influence the work reported in this paper.

□The authors declare the following financial interests/personal relationships which may be considered as potential competing interests.

Acknowledgments

Hayat Zanane is the owner of a PROFAS B^+ French-Algerian fellowship program.

Appendix A. Supplementary data

Supplementary data to this article can be found online at https://doi.org/10.1016/j.optmat.2019.01.066.

References

[1] C. Duverger, M. Bouzaoui, S. Turrell, J. Non-Cryst. Solids 220 (2–3) (1997) 169.
[2] K. Muruganandam, M. Seshasayee, J. Non-Cryst. Solids 222 (1997) 131.
[3] P. Charton, P. Armand, J. Non-Cryst. Solids 333 (3) (2004) 307.
[4] A. de Pablos-Martín, A. Duran, M.J. Pascual, Int. Mater. Rev. 57 (3) (2012) 165–186.
[5] K. Selvaraju, K. Marimuthu, J. Lumin. 132 (5) (2012) 1171.
[6] K. Annapoorani, K. Maheshvaran, S. Arunkumar, N. Suriya Murthy, K. Marimuthu, Spectrochim. Acta A. Mol. Biomol. Spectr. 135 (14) (2015) 1090.
[7] M.A. Khaled, H. Elzahed, S.A. Fayek, M.M. El-Ocker, Mater. Chem. Phys. 37 (4) (1994) 329.
[8] I. Jlassi, H. Elhouichet, M. Ferid, Mater. Sci. 46 (3) (2011) 806.
[9] E.S. Nurbaisyatul, K. Azman, H. Azhan, W.A.W. Razali, A. Noranizah, S. Hashim, Opt. Spectra 116 (3) (2014) 413.
[10] S. Sakida, S. Hayakawa, T. Yoko, J. Non-Cryst. Solids 243 (1) (1999) 13.
[11] S. Yousef, J. Alloy. Comp. 561 (5) (2013) 234.
[12] H. Burger, W. Vogel, Infrared Phys. 25 (1–2) (1985) 395.
[13] K. Hirao, S. Kishimoto, K. Tanaka, S. Tanabe, N. Soga, J. Non-Cryst. Solids 139 (1992) 151.
[14] K. Shioya, T. Komatsu, H.G. Kim, R. Sato, K. Matusita, J. Non-Cryst. Solids 189 (1–2) (1995) 16.
[15] Z. Pan, S.H. Morgan, J. Non-Cryst. Solids 210 (2–3) (1997) 130.
[16] J.A. Anjaiah, C. Laxmikanth, N. Veeraiah, Phys. B Condens. Matter 454 (1) (2014) 148.
[17] J. Fu, J.M. Parker, P.S. Flower, R.M. Brown, Mater. Res. Bull. 37 (2002) 1843.
[18] X. Qiao, X. Fan, M. Wang, J.-L. Adam, X. Zhang, J. Phys. Condens. Matter 18 (2006) 6937–6951.
[19] M. Secu, C.E. Secu, S. Polosan, G. Aldica, C. Ghica, J. Non-Cryst. Solids 355 (2009) 1869–1872.
[20] M. Pokhrel, G.A. Kumar, S. Balaji, R. Debnath, D.K. Sardar, J. Lumin. 132 (8) (2012) 1910.
[21] E.F. Chillcce, I.O. Mazali, O.L. Alves, L.C. Alves, Opt. Mater. 33 (3) (2011) 389.
[22] U.R. Rodríguez-Mendoza, E.A. Lalla, J.M. Cáceres, F. Rivera-López, S.F. León Luís, V. Lavín, J. Lumin. 131 (6) (2011) 1239.
[23] V. Nazabal, S. Todoroki, A. Nukui, T. Matsumoto, S. Suehara, T. Hondo, J. Non-Cryst. Solids 325 (1–3) (2003) 85.
[24] P. Veber, M. Velázquez, V. Jubera, S. Pechev, O. Viraphong, CrystEngComm 13 (16) (2011) 5220–5225.
[25] A. Jain, R. Pankajavalli, R. Babu, S. Anthonysamy, J. Therm. Anal. Calorim. 115 (2014) 1279–1287.
[26] T.S. Lakshmi Narasimhan, M. Sai Baba, R. Viswanathan, Thermochim. Acta 427 (1–2) (2005) 137–147.
[27] H. Zhao-xia, L. Hang-xin, X. Zhao-lu, W. Mei-han, H. Xiao-dan, W. Shao-hong, J. Alloy. Comp. 640 (2015) 311.
[28] Z. Zhao-xia Hou, Zhao-lu Xue, Shao-hong Wang, J. Alloy. Comp. 514 (2012) 109.

[29] Z. Hu, Y. Wang, E. Ma, F. Bao, Y. Yu, D. Chen, Mater. Res. Bull. 41 (2006) 217.
[30] Y. Kishi, S. Tanabe, S. Tochino, G. Pezzotti, Am. Ceram. Soc. 88 (12) (2005) 3423.
[31] G. Aldica, M. Secu, J. Non-Cryst. Solids 356 (2010) 1631.
[32] M. Kemere, J. Sperga, U. Rogulis, G. Krieke, J. Grube, J. Lumin. 181 (2017) 25.
[33] X. Sun, S.M. Huang, Nucl. Instrum. Methods Phys. Res. 621 (2010) 322.
[34] J. Cai, Xiantao Wei, F. Hu, Z. Cao, L. Zhao, Y. Chen, C. Duan, M. Yin, Ceram. Int. 42 (2016) 13990.
[35] P. Scherrer, Nach. Gesell. Wissens. Gott, Math. Phys. (1–2) (1918) 96.
[36] G.K. Williamson, W.H. Hall, Acta (1) (1953) 22.
[37] W. Bragg, Roy. Soc. London, Ser. A 89 (1914) 468.
[38] Nalt.Bur.Stand. (U.) Monogr.25. 21 (1985) 52.
[39] A. Peña-Revellez, P. Camy, A. Benayad, J.-L. Doualan, C. Maurel, M. Olivier, V. Nazabal, R. Moncorgé, Opt. Mater. 33 (11) (2011) 1616–1620.
[40] D.E. McCumber, Phys. Rev. A. 136 (1964) 954.
[41] B.F. Aull, H.P. Jenssen, IEEE J. Quant. Electron. QE 18 (1982) 925.
[42] S.A. Payne, L.L. Chase, L.K. Smith, W.L. Kway, IEEE. Quant. Electron. QE 28 (1992) 2619.
[43] E. Snitzer, E.M. Vogel, J.S. Wang, U.S. Patent, 1993, p. 5251062.
[44] J.S. Wang, E.M. Vogel, E. Snitzer, Opt. Mater. 3 (3) (1994) 187–203.
[45] A.N. Moiseev, A.V. Chilyasov, V.V. Dorofeev, O.A. Vostrukhin, E.M. Dianova, B.G. Plotnichenko, V.V. Koltashev, J. Optoelectron. Adv. Mater. 7 (4) (2005) 1875–1879.
[46] M.F. Churbanov, A.N. Moiseev, A.V. Chilyasov, V.V. Dorofeev, I.A. Kraev, M.M. Lipatova, T.V. Kotereva, E.M. Dianov, V.G. Plotnichenko, E.B. Kryukova, Phys. Chem. Glasses Eur. J. Glass Sci. Technol. B 49 (6) (2008) 297–300.
[47] A.S. Lobanov, G.E. Snopatin, A.M. Kutyin, V.V. Dorofeev, V.S. Polyakov, A.I. Suchkov, M.F. Churbanov, V.G. Plotnichenko, V.V. Koltashev, E.M. Dianov, Glass Phys. Chem. 38 (3) (2012) 274–279.
[48] A. Lin, A. Zhang, E.J. Bushong, J. Toulouse, Optic Express 17 (19) (2009) 16716–16721.
[49] M.F. Churbanov, A.N. Moiseev, A.V. Chilyasov, V.V. Dorofeev, I.A. Kraev, M.M. Lipatova, T.V. Kotereva, E.M. Dianov, V.G. Plotnichenko, E.B. Kryukova, J. Optoelectron. Adv. Mater. 9 (10) (2007) 3229–3234.
[50] H. Ebendorff-Heidepriem, K. Kuan, M.R. Oermann, K. Knight, T.M. Monro, Opt. Mater. Express 2 (4) (2012) 432–442.
[51] V.V. Dorofeev, A.N. Moiseev, M.F. Churbanov, T.V. Kotereva, A.V. Chilyasov, I.A. Kraev, V.G. Pimenov, L.A. Ketkova, E.M. Dianov, V.G. Plotnichenko, A.F. Kosolapov, V.V. Koltashev, J. Non-Cryst. Solids 357 (11–13) (2011) 2366–2370.
[52] T. Kosuge, Y. Benino, V. Dimitrov, R. Sato, T. Komatsu, J. Non-Cryst. Solids 242 (2–3) (1998) 154–164.
[53] M.D. O'Donnell, C.A. Miller, D. Furniss, V.K. Tikhomirov, A.B. Seddon, J. Non-Cryst. Solids 331 (1–3) (2003) 48–57.
[54] X. Feng, W.H. Loh, J.C. Flanagan, A. Camerlingo, S. Dasgupta, P. Petropoulos, P. Horak, K.E. Frampton, N.M. White, J.H.V. Price, H.N. Rutt, D.J. Richardson, Optic Express 16 (18) (2008) 13651–13656.
[55] F. Auzel, Ann. Télécom. 24 (5–6) (1969) 199.
[56] Frédéric Druon, Matias Velázquez, Philippe Veber, Sylvie Janicot, Oudomsack Viraphong, Buşe Gabriel, Marwan Abdou Ahmed, Thomas Graf, Daniel Rytz, Patrick Georges, Optic Lett. 38 (20) (2013) 4146–4149.
[57] Matias Velázquez, Philippe Veber, Buşe Gabriel, Yannick Petit, Philippe Goldner, Véronique Jubera, Daniel Rytz, Anaël Jaffres, Mark Peltz, Volker Wesemann, Patrick Aschehough, Gérard Aka, Opt. Mater. 39 (2015) 258–264.
[58] E. Nakazawa, S. Shionoya, Phys. Rev. Lett. 25 (25) (1970) 1710.
[59] F. Auzel, Proc. IEEE 61 (6) (1973) 758–786.
[60] F. Auzel, C.R. Acad, Sci. Paris 262 (1966) 1016.
[61] F. Auzel, C.R. Acad, Sci. Paris 263 (1966) 819.
[62] R. Buisson, J.-C. Vial, J. Phys., Lett. 42 (1981) L115.
[63] J.H. Van Vleck, In the Theory of Electric and Magnetic Susceptibilities, Oxford University Press, 1932, pp. 235–236 see more particularly pages.